GPPS | JOURNAL

JOURNAL OF THE GLOBAL POWER AND PROPULSION SOCIETY
journal.gpps.global

Loss Assessment of the Axial-Gap Size Effect in a Low-Pressure Turbine

Original article

Article history:
Submission date: 16 December 2019
Final revision date: 4 September 2020
Accepted date: 24 September 2020
Publication date: 26 January 2021

This is the updated version of a paper originally presented at the Global Power and Propulsion Technical Conference, GPPS Beijing19, in Beijing, Sept. 16–18 2019.

*Correspondence:
MO: oettinger@tfd.uni-hannover.de

Peer review:
Single blind

Keywords:
Axial turbines; turbine efficiency; axial gap; loss breakdown; CFD

Citation:
Oettinger M., Mimic D., Henke M., Schmunk O., and Seume J. R. (2020). Loss Assessment of the Axial-Gap Size Effect in a Low-Pressure Turbine. Journal of the Global Power and Propulsion Society. 5: 1–14.
https://doi.org/10.33737/jgpps/127834

Marcel Oettinger[1,*], Dajan Mimic[1], Michael Henke[1], Oleg Schmunk[2], Joerg R. Seume[1]

[1]*Institute of Turbomachinery and Fluid Dynamics, Leibniz Universität Hannover, Appelstrasse 9, 30167 Hanover, Germany*
[2]*MTU Aero Engines AG, Dachauer Strasse 665 80995 Munich, Germany*

Abstract

The aim of this work is the decomposition, quantification, and analysis of losses related to the axial-gap size effect in a 1.5-stage low-pressure turbine. Both experimental data and unsteady RANS calculations are investigated for axial gaps equal to 20%, 50% and 80% of the stator axial chord. A framework for identifying sources of loss typically encountered in turbomachinery is derived and utilized for the low-pressure turbine presented. The analysis focuses on the dependency between these losses and the axial-gap variation. It is found that two-dimensional profile losses increase for smaller gaps due to higher wake-mixing losses and unsteady wake-blade interaction. Losses in the end-wall regions, however, decrease for smaller gaps. The total system efficiency can be described by a superposition of individual loss contributions, the optimum of which is found for the smallest gap investigated.

It is concluded that these loss contributions are characteristic for the medium aspect-ratio airfoils and operating conditions investigated. This establishes a deeper physical understanding for future investigations into the axial-gap size effect and its interdependency with other design parameters.

Introduction

The axial spacing between moving and stationary rows has been a major focus of research over the past years. This trend is driven by the need to optimize unsteady blade-row interaction and meeting design goals such as more compact components and reduced weight.

The axial-gap size affects the intensity of intra-row secondary flow, wake and potential interactions. Pressure fluctuations between moving and stationary rows can be subdivided into a uniformly steady component, a steady component relative to the reference frame of the stator and a steady component relative to the reference frame of the rotor. According to Jung (2000), the component which is steady relative to one frame acts as an unsteady fluctuation relative to the other component.

Praisner et al. (2006) argued that a larger axial gap would be beneficial regarding system loss, as the wakes mix out to a higher degree before they are affected by dilation resulting in higher loss. The wake impinging upon the leading edge of a downstream blade can result in increased incidence and can induce bypass transition, see, e.g., Coull and Hodson (2011); the intensity of both effects is inversely proportional to the axial-gap size.

For three-dimensional flow, however, secondary flow caused by the end-wall boundary layers has to be considered as well. As a result of the losses induced by secondary-flow vortices, as described by, e.g., Denton (1993), smaller axial gaps appear beneficial in this regard.

At the mid-span, Pichler et al. (2017) were able to identify higher losses for smaller axial gaps using quasi three-dimensional LES simulations. Because of decreasing potential-field-interaction effects and resulting lower wake dilation, the production of turbulent kinetic energy decreases, thus confirming the arguments of Praisner et al. (2006).

For a shrouded rotor with an aspect ratio of AR = 2.3, Yamada et al. (2009) found an optimal gap of 37% stator chord at the design point. The near-hub losses increased with axial-gap size and the tip-region losses decreased because of stronger and weaker passage vortices, respectively.

In the studies conducted by Restemeier et al. (2013) and Gaetani et al. (2010), secondary-flow intensity was the dominant factor driving system loss. Both of the turbines investigated feature comparatively small aspect ratios and an unshrouded design, resulting in higher secondary-flow losses compared to profile losses. An optimum was found at a gap equal to 50% of the stator axial chord. Similarly, Park et al. (2003) observed higher efficiency for a smaller axial gap due to the decreasing intensity of secondary flow.

While the basic aspects of the axial-gap size effect – end-wall losses tend to increase with gap size, while profile losses typically decrease – are generally well-understood, a strong disagreement regarding the influence of axial-gap size on the total system loss can be identified in the literature. One reason for conflicting results is the general interdependency of the loss contributions as well as the axial-gap size effect correlating with secondary design parameters. Bellucci et al. (2017) found a strong interdependency of axial-gap-related losses with both aspect ratio and inlet Reynolds number. In a review of the literature, Grönman et al. (2014) were able to correlate the axial-gap size effect with secondary design parameters like the pitch-to-axial-chord ratio of the stator, circumferential Mach number, and the rotor aspect ratio. Additional dependencies, such as the rotor being shrouded or unshrouded, cavity design or blade loading, are likely to exist as well. Transonic flow and the presence of shock waves strongly affects loss generation and its dependency on gap size too (Venable et al. 1999).

Utilizing both experimental data and numerical results obtained from unsteady RANS calculations, this paper aims to show the development and sources of loss for three different axial gaps. Accounting separately for individual loss contributions in a quantitative manner forms the basis for future investigations into the interdependency of the axial-gap size effect with other design parameters and operating conditions. To this end, the present paper will answer the following three questions:

1. How does the total loss relate to the axial gap?
2. How do individual loss contributions depend on gap size?
3. What are the underlying physical effects?

Loss analysis

The most accurate and robust method to quantify loss is the assessment of the total amount of entropy present in a thermodynamic system.

Since the system considered is modeled using adiabatic wall boundaries, entropy as per

$$s = c_p \ln\left(\frac{T}{T_{\mathrm{ref}}}\right) - R \ln\left(\frac{p}{p_{\mathrm{ref}}}\right) \tag{1}$$

lends itself as the base quantifier of flow losses. In order to distinguish the losses according to their generating flow phenomena, distinct quantities for identification are needed. The distinction between different sources of entropy is based purely on phenomenological criteria and not on physical entropy-generating mechanisms, i.e., the losses are distributed amongst profile boundary layers, wakes, end-wall boundary layers (hub and tip), and secondary flow.

A common feature which all these flow phenomena share, is that they exist in flow regions where the vorticity $\vec{\omega} = \vec{\nabla} \times \vec{c}$ does not equal zero. The first distinction can be made between secondary flow and boundary layers as well as wakes. Secondary flow consists of vortex structures which can be characterized by their streamwise vorticity

$$\omega_{\mathrm{SW}} = \frac{\vec{\omega} \cdot \vec{c}}{|\vec{c}|}, \tag{2}$$

which is the projection of the vorticity vector onto the local velocity vector. Using the Pythagorean Theorem, the vorticity vector can be decomposed into a streamwise and a crosswise component perpendicular to the local flow direction

$$\vec{\omega} \cdot \vec{\omega} = \omega^2 = \omega_{\mathrm{SW}}^2 + \omega_{\mathrm{CW}}^2. \tag{3}$$

The crosswise vorticity is characteristic for boundary layers, wakes, and rotational shear layers in general. Based upon these considerations, the following blending factors can be formulated:

$$w_{\mathrm{SW}} = \frac{\omega_{\mathrm{SW}}^2}{\max(\omega^2,\, 1 \times 10^{-16})} \tag{4}$$

and

$$w_{\mathrm{CW}} = \frac{\omega_{\mathrm{CW}}^2}{\max(\omega^2,\, 1 \times 10^{-16})}. \tag{5}$$

The subdivision between boundary layers on the end wall or profile and wakes, however, necessitates additional blending factors. To discriminate between end-wall and profile boundary layers or wakes, the vorticity in cylindrical coordinates $\vec{\omega} = (\omega_x,\ \omega_r,\ \omega_\theta)^T$ is used and the following differentiation between cases is defined:

$$\psi_r(\vec{\omega}) = \begin{cases} 1 & \text{if} \quad \omega_r^2 > (\omega_x^2 + \omega_\theta^2), \\ 0 & \text{else.} \end{cases} \tag{6}$$

Here, $\psi_r(\vec{\omega})$ represents a Boolean function, which is "true" or unity, when the local vorticity vector is of predominantly radial orientation, i.e., in the profile boundary layers and wakes. The entropy due to crosswise vorticity of radial orientation is

$$s_{\mathrm{CW},r} = w_{\mathrm{CW}} \psi_r s \tag{7}$$

and

$$s_{\mathrm{CW},\neg r} = w_{\mathrm{CW}} (1 - \psi_r) s \tag{8}$$

for a deviating orientation of the vorticity vector.

To further isolate the profile boundary layers from the wakes, a distinction is made, based upon the distance normal to the profile d_{P}:

$$\psi_{\mathrm{P}}(d_{\mathrm{P}}) = \begin{cases} 1 & \text{if} \quad d_{\mathrm{P}} \leq \delta_{\max} \\ 0 & \text{else.} \end{cases} \tag{9}$$

The critical distance of $\delta_{\max} = 0.6$ mm is chosen, which is the maximum boundary layer thickness across all blades of the present configuration.

Regions, where $\psi_r(\vec{\omega})$ returns "false" or zero are consequently characterized by predominantly axial-circumferential vorticity. This is the case in the end-wall boundary layers. But also in some parts of the wakes, as they interact with secondary flow and experience twisting amongst the longitudinal axis of the secondary-flow vortices. The separation between hub and tip boundary layer and the part due to wakes is defined by the relative radial height $(r - r_{\min})/H$:

$$\psi_{\mathrm{H}}\left(\frac{r - r_{\min}}{H}\right) = \begin{cases} 1 & \text{if} \quad \dfrac{r - r_{\min}}{H} < 0.15 \\ 0 & \text{else.} \end{cases} \tag{10}$$

and

$$\psi_{\mathrm{T}}\left(\frac{r-r_{\min}}{H}\right)=\begin{cases}1 & \text{if} \quad \dfrac{r-r_{\min}}{H}>0.90\\ 0 & \text{else.}\end{cases} \tag{11}$$

The regions between $(r-r_{\min})/H=0.15$ and $(r-r_{\min})/H=0.90$ are included in the wake losses. The individual contributions to the overall entropy are, therefore, defined as follows:
The contribution of the secondary flow is given by

$$s_{\mathrm{SW}}=w_{\mathrm{SW}}s; \tag{12}$$

the profile boundary layer by

$$s_{\mathrm{CW,P}}=w_{\mathrm{CW}}\psi_{\mathrm{P}}\psi_{r}s; \tag{13}$$

the hub boundary layer by

$$s_{\mathrm{CW,H}}=w_{\mathrm{CW}}(1-\psi_{\mathrm{P}})(1-\psi_{r})\psi_{\mathrm{H}}s \tag{14}$$

the tip boundary layer by

$$s_{\mathrm{CW,T}}=w_{\mathrm{CW}}(1-\psi_{\mathrm{P}})(1-\psi_{r})\psi_{\mathrm{T}}s \tag{15}$$

and the contribution of the wakes is determined by

$$s_{\mathrm{CW,W}}=w_{\mathrm{CW}}(1-\psi_{\mathrm{P}})(1-\psi_{\mathrm{H}})(1-\psi_{\mathrm{T}})s \tag{16}$$

Each individual loss contribution is then integrated over the main flow domain, i.e., the turbine excluding the cavities, to obtain the resulting total,

$$S_i=\iiint_{\nu}\rho s_i \mathrm{d}V \tag{17}$$

The approach shown here is also used to assess the loss contribution of shock-wave vortex interaction in Mimic et al. (2019) where it is found to produce similarly satisfactory results.

Test case

The general flow field of the present 1.5-stage turbine configuration was investigated previously by Henke et al. (2016) and Biester et al. (2013). A primary goal of this turbine design was to ensure a homogeneous flow field in the mid-span unaffected by the end walls. It is therefore suitable for quantifying losses according to the decomposition above.

Turbine configuration

The turbine is a low-pressure turbine with an aspect ratio of AR = 2.15 as described by Henke et al. (2016). Both stator rows can be moved in axial direction as well as be circumferentially clocked independently from each other, see Henke et al. (2012). Three different axial gaps were chosen for experimental investigation. The gap sizes X are equal to 20%, 50% and 80% of the stator axial chord, respectively. Axial spacings are adjusted in unison for both the stator-rotor and rotor-stator gap. The clocking is adjusted together with the axial-gap variation by changing the circumferential positions of the stator-blade rows relative to each other. This yields a similar incoming wake distribution relative to the blades and enables the isolation of the axial-gap size effect: An imaginary particle originating from the stator 1 trailing edge impinges upon the stator 2 leading edge for all configurations. As the blade count of stator 2 is double that of stator 1 (Tab. 1), only every second blade of the stator 2 passage is directly affected by the stator 1 wake flow.

Table 1. Test conditions and stage characteristics

Rotational speed n in 1/min		6950	
Inlet total pressure $p_{t,in}$ in kPa		168.6	
Inlet total temperature $T_{t,in}$ in K		344.2	
Mass flow rate $\dot{m}$ in kg/s		8.9	
Total pressure ratio Π_t		1.42	
	Stator 1	Rotor	Stator 2
Number of blades	18	30	36
Aspect ratio AR	2.15	2.15	2.15
Reynolds number Re	$7.5{\cdot}10^5$	$6.5{\cdot}10^5$	$4.2{\cdot}10^5$

Detailed aerodynamic characteristics and a base verification of the overall time-averaged flow field can also be found in Henke et al. (2016).

Instrumentation

The instrumentation of the experimental setup has been devised in order to answer the questions posed in the introduction of this paper in terms of time-accurate and time-averaged measurements of the local flow conditions.

To quantify the overall efficiency, rake probes measuring total pressure and total temperature at the inlet and outlet as well as pressure instrumentation on the blade surfaces were designed during a numerical pre-test analysis, including a local optimization of measurement positions.

Figure 1 shows a sectional view of the flow path including the measurement planes (MP). MP00, which is located further upstream of the control volume and thus not shown here, features equally spaced rake probes to verify the homogeneous, swirl free inlet flow of the turbine on a grid of six circumferential rakes with six radial positions each. Rake probes in MP32 have been designed to deliver a 360 deg record of total quantities as well as the static pressure and swirl angle. In order to operate these rakes in the three-dimensional flow field downstream of stator 2, the kiel-head probes have been designed with a pre-twist in order to record accurate data of the local flow-field for all radial measurement positions.

As these rake probes provide only limited radial resolution of the flow field, additional five-hole-probe measurements have been conducted in the measurement planes MP10 (inlet section) and MP31 (outlet section). While rake probes allow continuous data acquisition, probe traverses provide better resolution in radial direction

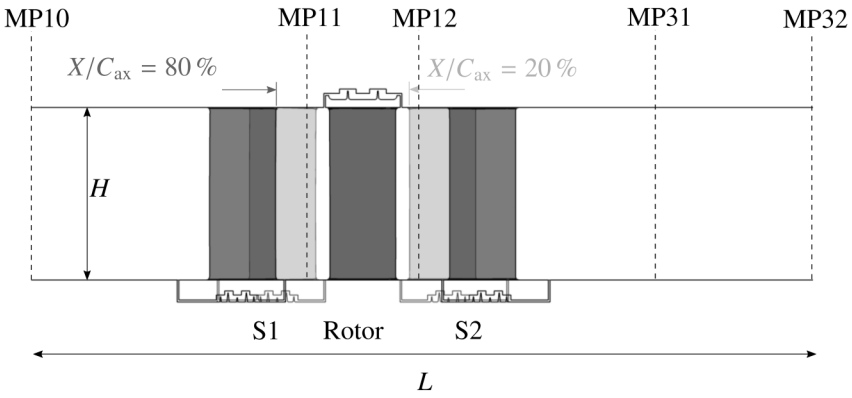

Figure 1. Schematic of the 1.5-stage turbine test rig. Small gap $X/C_{ax} = 20\%$ in light gray; large gap $X/C_{ax} = 80\%$ in dark gray.

for a specific point in time. A combination of these data sources provides a set of high-resolution boundary conditions for each experiment, which are used in the present work. Within the stator-rotor and rotor-stator gap regions between the blade rows, time-averaged as well as time-resolved multi-hole-probe traverses were conducted for the medium and large axial-gap configuration. For the smallest gap investigated, the remaining gap between two blade rows is too small for probe measurements. Therefore, the blading itself has been equipped with pressure taps (time-averaged and time-accurate wall taps) on the suction and pressure sides and in the leading and trailing edges. This allows determining the wake-flow properties and unsteady flow characteristics for all three axial-gap configurations.

Numerical setup

The experimental data is supplemented by steady and unsteady RANS calculations for all three gaps using the TRACE solver, which is being developed by the German Aerospace Center (DLR) in cooperation with MTU Aero Engines AG. The general numerical setup used in this work is mostly identical to the ones described by Henke et al. (2016) and Biester et al. (2012). The following short summary will focus on modifications to the referenced setups.

For steady-state calculations, mixing planes are positioned at 50% of the axial gap. For unsteady simulations, one blade passing period (BPP) is resolved by 192 time steps; each time step is resolved using 30 sub-iterations. A Courant-Friedrichs-Levy (CFL)-number of 50 is used for all calculations. As a result of the blade counts detailed in Tab. 1, a periodic 60 deg segment is used for the simulations. The k-ω-model by Wilcox (1998) with the extension by Kato and Launder (1993) to correct the turbulent-kinetic-energy production near the stagnation point is used to model the effect of turbulence. The extension of Bardina et al. (1985) is used to account for rotational effects. A multi-mode transition model as devised by Kožulović et al. (2007) is used to model transition. Viscous walls in the main flow domain utilize a low-Reynolds formulation of the turbulence model. Walls inside the cavities are not resolved; instead, wall functions are used locally.

To assess convergence, the fluctuating pressure signal at several point probes inside the computational domain is evaluated. Convergence is reached when the maximum amplitude deviation between two periods is below a threshold of $\Delta p = 0.1\%$. Apart from static pressure – which is area-averaged – all flow variables are mass-flow-averaged across the specified planes.

Flow field analysis

In line with the introductory discussion, the flow field is decomposed into a quasi-two-dimensional flow at the mid-span and three-dimensional flow across the entire span. In order to obtain a better understanding of the loss evolution, axial distributions are considered as well.

Axial distributions

Figure 2 depicts the axial distribution of the circumferentially and spanwise-averaged entropy for all gaps. Four regions of interest are identified:

1. Stator 1: Losses are initially proportional to the flow path length upstream of the stator 1 leading edge. Downstream of the first stator, losses increase initially for larger axial gaps as a result of increased secondary-flow and wake-mixing losses.
2. Rotor: All axial gaps show a nearly identical slope in entropy increase. For the smallest gap, total losses at the rotor trailing edge are substantially lower than for the other gaps.
3. Stator 2: Due to the stronger wake-boundary-layer interaction at the second stator, losses increase for the smaller gaps.
4. Flow downstream of stator 2: Wakes and vortices mix out increasingly, resulting in linearly increasing losses. The slope is flat relative to the absolute difference between axial gaps, i.e., compensating smaller axial gaps with an outlet further upstream – as would be the case for neighboring components in a real machine – does not result in equal total system loss.

Since cavities are not included in the post-processing control volume, entropy fluctuations at the cavity inlets and outlets can be observed, which can also result in a local entropy decrease in the main flow domain. Generally speaking, the entropy increase is steepest in the rotor and stator passages, whereas it is less pronounced outside of the blading. Minimum system loss occurs for the smallest axial gap, while the losses are highest for the largest gap examined. The underlying physical effects are investigated below in further detail.

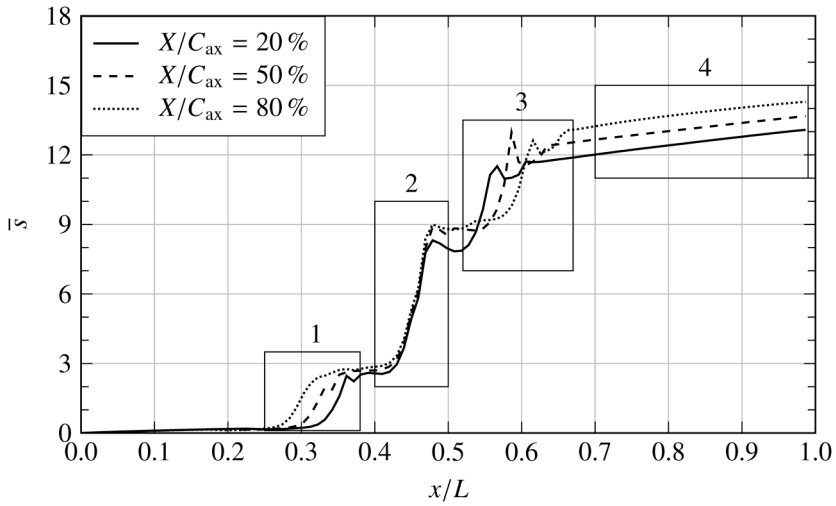

Figure 2. Axial distributions of time-averaged entropy (URANS calculations).

Two-dimensional flow field

For the quasi two-dimensional flow field at the mid-span, profile losses are the dominant factor. Instantaneous entropy contours at different time steps are pictured in Figure 3 to visualize the wakes for the small and large

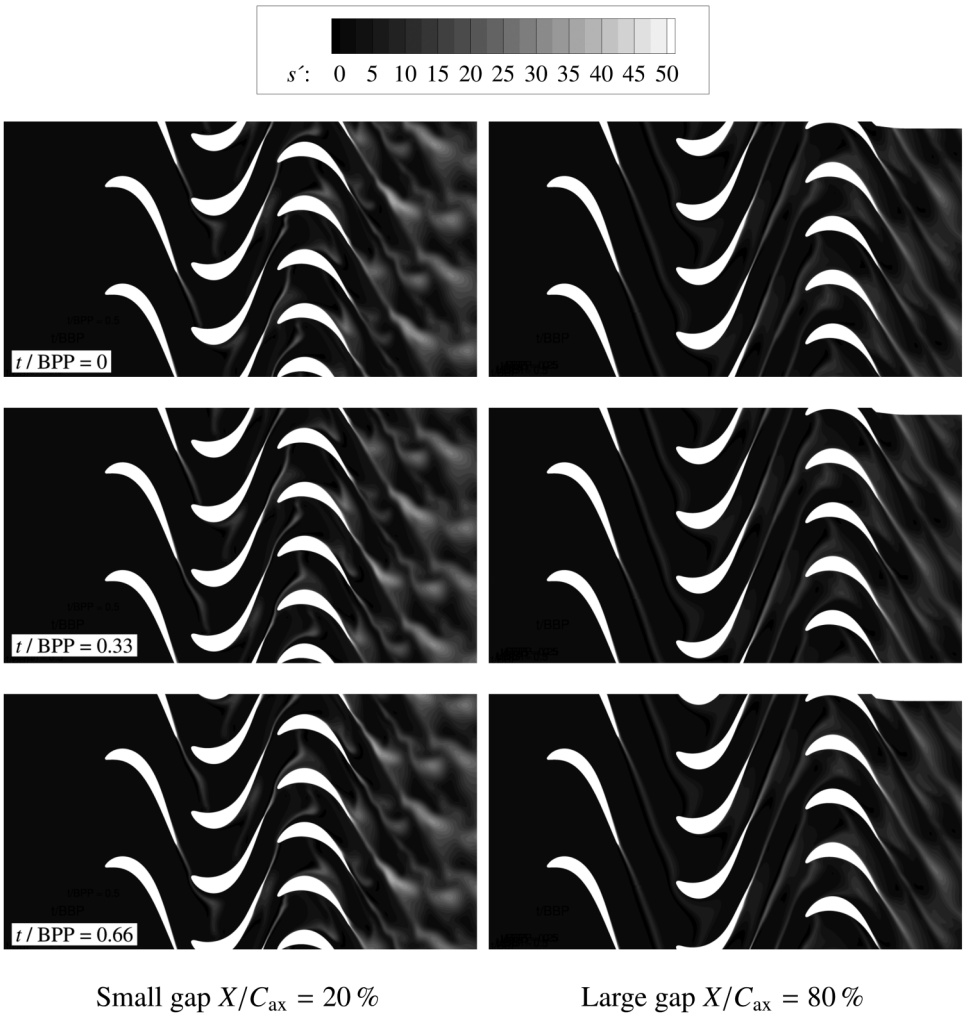

Figure 3. Instantaneous entropy contours at mid-span (URANS).

gaps. The low-momentum wakes of the first stator enter the rotor, experience dilation and are transported into the second stator frame. Because of the comparatively high turning, an increase in axial gap affects the wake mixing process disproportionately. For the large axial gap, the wake is almost entirely mixed out when entering the rotor, the same is true for the rotor wakes entering the second stator. For the small gap, wakes are deflected by the leading edge of the downstream row almost as soon as they are shed: A strong interaction of the wake with the potential field of the downstream row can be inferred. Downstream of the second stator, a highly unsteady flow field can be identified, which is caused by the comparatively strong wake-inducing periodic fluctuations on the suction side: Wakes of varying intensity are shed. As a result, entropy production at the mid-span increases considerably for the smallest axial gap. This evaluation is consistent with the two-dimensional prediction of Praisner et al. (2006).

Three-dimensional flow field

The essential aspects of the three-dimensional flow field in the form of circumferentially averaged flow variables were presented by Henke et al. (2016). Figure 4 depicts distributions of streamwise vorticity in measurement plane (MP) 12. With the distance between rotor trailing edge and MP12 remaining constant despite gap variation, both gaps show only minor differences regarding secondary flow, represented here by the streamwise vorticity and the streamwise loss component s_{SW}. The circumferential extent of the hub passage vortex increases slightly for the large gap case, reflecting its dependency on the upstream flow conditions. Regarding wake-related losses in the mid-span region, as represented by the crosswise loss component s_{CW}, a slight increase is found for the medium gap. This is due to the smaller axial gaps increasing the wake interaction between the upstream stator and the rotor, as is also evident in Figure 3. This results in an entropy increase being transported downstream by the wake. The functional decomposition of entropy using the streamwise and crosswise vorticities is capable of identifying individual sources of loss. The hub and tip wall boundary layers are captured using s_{CW}.

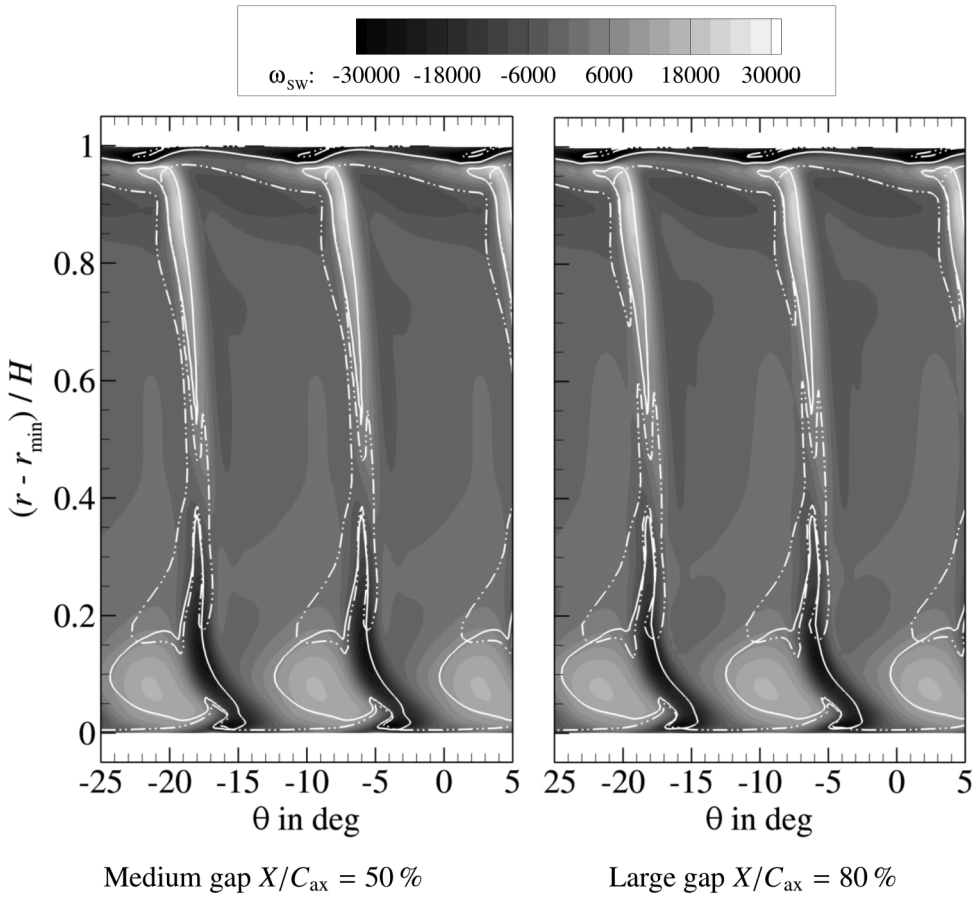

Figure 4. Time-averaged flow field downstream of the rotor (MP12, URANS). Dash-dotted lines denote s_{CW}; solid lines s_{SW}.

In the presence of trailing shed vortices, an overlap of both contributions exists in the wake region. An interaction between the vortices and the wakes can be inferred, as the streamwise loss component virtually cuts into the crosswise-dominated region. The presence of s_{SW} in the tip region is a result of shroud leakage flow re-entering the main flow.

Figure 5 depicts the distribution of the circumferentially averaged streamwise vorticity downstream of the second stator. Additionally, a single contour line of the loss contribution $s_{CW,r}$, representing the crosswise loss component not aligned in the radial direction, is shown. Naturally, $s_{CW,r}$ is non-zero at the end walls, allowing for the identification of end-wall boundary layer related losses. Of particular relevance is the shear layer caused by the cavity-main-flow interaction at the hub, which merges with the boundary layer and is identified as the main driver for the end-wall losses. End-wall-related losses therefore increase with gap size and the hub-related contribution is higher than the tip-related contribution. Despite $s_{CW,r}$ being, by definition, equal to zero if the local vorticity vector is oriented in radial direction – as is the case for ideal, two-dimensional profile boundary layers and wakes – a non-zero contribution of this fraction can be identified in the mid-span region.

Additional spots of increased $s_{CW,r}$ are visible in the lower third just adjacent to the hub-wall boundary layer. Here, the wakes interacting with the vortices result in vortex deflection where the vortices are virtually cut by the passing wake, as mentioned before. This causes a torsion of the wake, which is the reason behind the non-zero contribution of $s_{CW,r}$ outside of the boundary layers. This effect is more pronounced for the smallest axial gap. As can be seen in Figure 3, the flow area influenced by the wake is much larger for the small gap as a result of the highly unsteady wake shedding at the second stator which exceedingly amplifies wake torsion and resulting vortex deflection. The spots of increased $s_{CW,r}$ near the hub merge with the hub boundary layer into one continuous flow region. This impedes a clear distinction between both individual effects. The blanking merely based on the radial distance to the end walls reveals potential for improvement of the loss decomposition proposed.

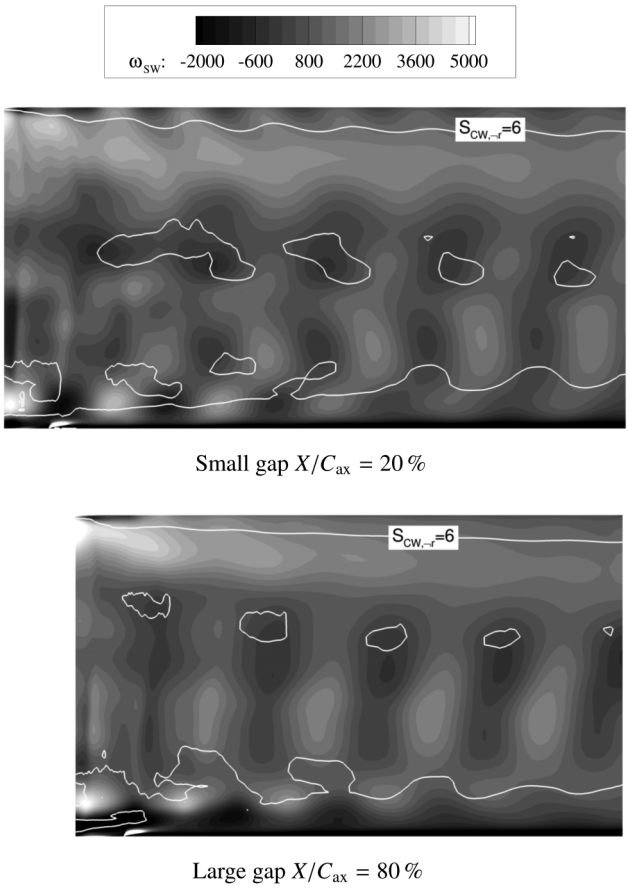

Figure 5. Circumferentially and time-averaged streamwise vorticity downstream of stator 2 featuring loss contribution $s_{CW,-r}$ (URANS).

Integral parameters

Loss analysis

Based upon the detailed flow analysis, losses are broken down in Figure 6. The present study shows that the total system loss increases with the axial-gap size. These results are consistent with Yamada et al. (2009), who investigated a similar turbine configuration. In the hub and tip regions, more pronounced boundary and shear layers from the cavity interaction increase losses for larger gaps. As is evident in Figure 5, the end-wall losses at the hub are higher than at the tip which is also reflected in Figure 6. The profile losses, i.e., the losses immediately caused by the blade boundary layers, are a negligible loss factor and remain almost constant regardless of the axial gap. Interestingly, wake losses also show little variation for a change in axial-gap size. As can be seen in the efficiency distribution in Figure 7, a greater flow-path length between the stator 2 trailing edge and the outlet – which results from a decrease in axial-gap size – leads to an increasing redistribution of total enthalpy from the mid-span into the end-wall regions. This effect is superposed by the aforementioned merging of the end-wall boundary layer and wake structures. Since wake-torsion losses are only accounted for between 15% and 90% of the channel height, as per the definition above, a redistribution into the boundary layers results in an underestimation of the wake-induced losses, i.e., wake losses are counted as end-wall losses in the loss decomposition proposed. This is due to the end-wall and wake-torsion losses being both represented by $s_{CW,r}$. A closer look at the wake losses at the mid-span between 40% and 70% of the channel height, which are labelled $S_{CW,MS}$ in Figure 6, reveals an increase in wake-induced losses inversely proportional to the axial gap; this is consistent with the observed increase in $s_{CW,\neg r}$ in the mid-span region (Figure 5) and the efficiency distribution in Figure 7. The exact cut-off between the end-wall and mid-span regions as well as the distinction between inter-merged effects can be improved for a better loss prediction.

The losses observed in the mid-span region can be subdivided into direct wake-blade interaction, mixing losses and wake torsion with resulting vortex deflection downstream of the blades. As shown in Figure 3, the maximum increase in entropy actually occurs downstream of stator 2 and not inside of the blade passages, leading to the conclusion that the latter two effects are dominant with regard to wake losses.

The nearly identical secondary-flow losses for the medium and large axial gap suggest that the small axial gap inhibits the formation of secondary-flow-vortex structures disproportionally. If the gap reaches a certain threshold, the secondary-flow losses remain mostly constant, the effect of the increased flow-path length is reflected in the end-wall boundary layer losses. Considering Figure 5 and the decomposition above, it can be argued that the increase in secondary-flow losses occurs primarily in the tip region downstream of the second stator. For the investigated aspect ratio and operating conditions, end-wall related losses (secondary flow and end-wall boundary layers) account for roughly 2/3 of the total losses.

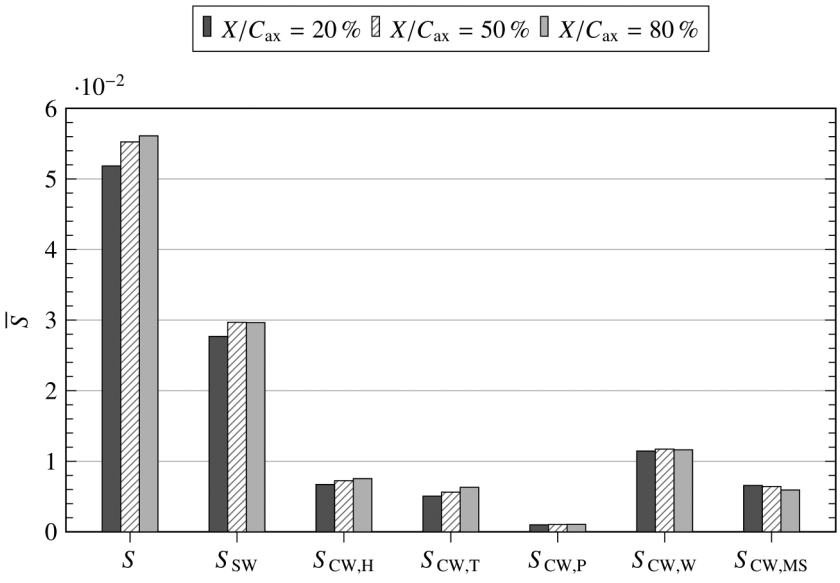

Figure 6. Loss contributions from time-averaged URANS.

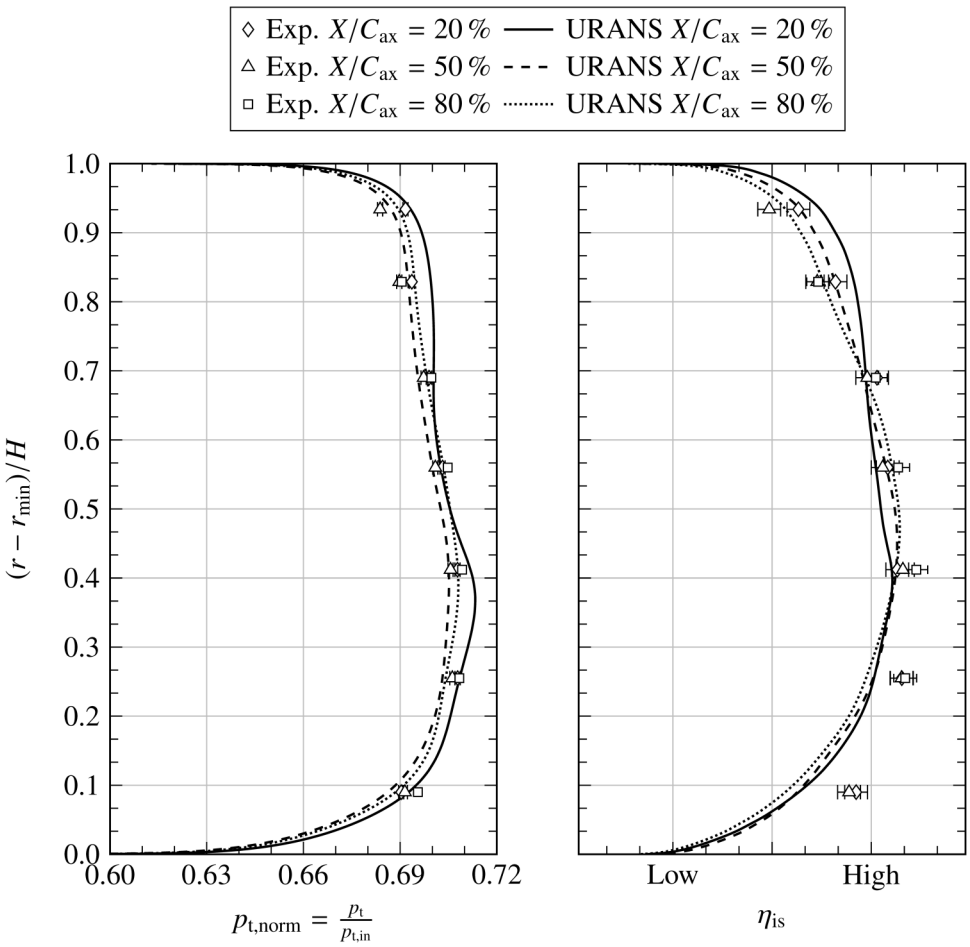

Figure 7. Circumferentially and time-averaged outlet flow field for axial gaps investigated.

System efficiency

Figure 7 depicts the flow field at the outlet of the control volume for all axial gaps investigated. Of note is the missing total-pressure measurement at 93% of the channel height for the large gap. As the total-pressure information is missing for 2 circumferential positions, no representative average can be calculated at this position. Because of this, and a similar error for the total temperature measurement at 9% of the channel height, no efficiency information at these positions can be given for the large-gap case. For the isentropic efficiency, a clear distinction of the axial-gap size effect depending on radial location can be identified in accordance with the loss breakdown presented: In the hub and tip regions, losses increase for larger gaps. While the hub region shows higher losses in general, the variation, i.e., the influence of the axial-gap size, is higher in the tip region than at the hub. In the region between 40% and 70% of the channel height an inverse trend can be identified, i.e., losses increase for smaller gaps. Of particular note is the aforementioned redistribution from the mid-span region towards the end-wall regions. The small-gap distributions are, therefore, more uniform compared to the larger gaps. The trends discussed apply to both numerical and experimental data although different predictive trends exist at some radial positions. While the good agreement in the total pressure distribution validates the loss breakdown above, the comparatively high measurement uncertainty, however, precludes a detailed assessment of the experimental efficiency distribution.

The resulting system efficiency is depicted in Figure 8. In addition to the URANS simulations, results from steady-state calculations are also considered. Despite steady-state CFD not capturing stator-rotor interaction, the overall trend does agree: The smallest gap investigated represents the optimum configuration.

Conclusions

The effect of the axial-gap size on system losses is quantified using a functional separation of different entropy sources, such as end-wall friction, profile loss, and secondary flow. For these individual terms, different trends with regard to axial-gap variation can be identified. For the quasi two-dimensional flow field in the mid-span

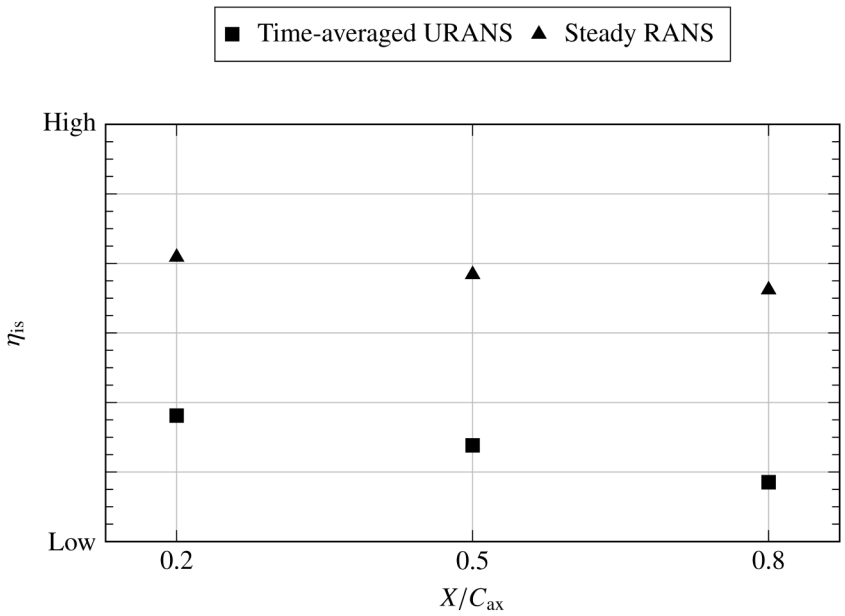

Figure 8. Total-to-total system efficiency.

region, larger axial gaps are beneficial due to the reduced wake dilation and associated mixing losses in the downstream row. For the smallest gap, unsteady wake-blade interaction is a major source of two-dimensional loss. A more extensive investigation of the flow region outside of the boundary layers revealed, however, that a clear distinction into two- and three-dimensional flow is valid only for a very small flow region at the mid-span. All other flow regions are afflicted by a strong interaction between – or even merging of – various phenomena, which are not just a superposition of multiple effects. In contrast to the trend immediately at the mid-span, end-wall regions show an increase in losses for larger axial gaps, due to higher friction and stronger secondary flow. End-wall related losses contribute almost 2/3 of the entire system loss: It is found to be the dominant loss contribution.

The optimal axial gap is, therefore, an ideal compromise between individual loss contributions for a given turbine configuration. For the configurations investigated, the optimal gap equals 20% of the stator axial chord length.

Based on the framework derived in the present work, the interdependency of the axial-gap size effect and secondary design parameters will be the subject of further research. It is, for example, self-evident that a higher aspect ratio would lead to profile losses becoming a more dominant factor, which would then shift the optimal gap towards a larger size. Nevertheless, a more refined distinction criterion between end-wall boundary-layer and wake flow should be derived before proceeding further.

Since the focus of this paper was the time-averaged flow field, instantaneous unsteady effects were generally neglected. Unsteady losses, therefore, remain a factor to be considered in greater detail.

Nomenclature

Latin symbols

AR aspect ratio
c velocity
C chord
d distance
H channel height
L total length of configuration
$\dot{m}$ mass flow rate
n rotational speed
p pressure
r radial coordinate

R gas constant
s specific entropy
S entropy
t time
T temperature
w blending factor
x axial coordinate
X axial spacing

Greek symbols

δ_{max} critical distance
ξ loss fraction
η efficiency
θ circumferential coordinate
μ viscosity
Π pressure ratio
ω vorticity
ψ boolean function

Subscripts

ax axial
CW crosswise
H hub
in quantity at inlet
is isentropic
max maximum
min minimum
norm normalized quantity
P profile
ref reference
SW streamwise
T tip
t total quantity
W wake

Operators

$\overline{[\,]}$ time-averaged quantity
$[\,]'$ instantaneous quantity
$\overrightarrow{[\,]}$ vector

Abbreviations

BPF blade passing frequency
BPP blade passing period
CFL Courant-Friedrichs-Levy
MP measurement plane
S stator
Re Reynolds number

Acknowledgements

We gratefully acknowledge the substantial contribution of the DLR Institute of Propulsion Technology and MTU Aero Engines AG for providing TRACE.

Funding sources

MTU Aero Engines AG.

Competing interests

Marcel Oettinger declares that he has no conflict of interest. Dajan Mimic declares that he has no conflict of interest. Michael Henke declares that he has no conflict of interest. Oleg Schmunk declares that he has no conflict of interest. Joerg R. Seume declares that he has no conflict of interest.

References

Bardina J., Ferziger J. H., and Rogallo R. S. (1985). Effect of rotation on isotropic turbulence: Computation and modelling. *Journal of Fluid Mechanics*. 154: 321–336. https://doi.org/10.1017/S0022112085001550.

Bellucci J., Rubechini F., Arnone A., Arcangeli L., Maceli N., et al. (2017). Numerical and experimental investigation of axial gap variation in high-pressure steam turbine stages. *Journal of Engineering for Gas Turbines and Power*. 139 (5). https://doi.org/10.1115/1.4035158.

Biester M. H., Henke M., Seume J. R., Guendogdu Y., and Engel K. (2012). Unsteady Wake-Blade Interaction: A Correlation Between Surface Pressure Fluctuations and Loss Generation. In: ASME Turbo Expo. Copenhagen: ASME, pp. 2743–2752. https://doi.org/10.1115/GT2012-69616.

Biester M. H.-O., Wiegmann F., Guendogdu Y., and Seume J. (2013). Time-Resolved Numerical Study of Axial Gap Effects on Labyrinth-Seal Leakage and Secondary Flow in a LP Turbine. In: ASME Turbo Expo. San Antonio: ASME. https://doi.org/10.1115/GT2013-95628.

Coull J. D., and Hodson H. P. (2011). Unsteady boundary-layer transition in low-pressure turbines. *Journal of Fluid Mechanics*. 681: 370–410. https://doi.org/10.1017/jfm.2011.204.

Denton J. D. (1993). Loss mechanisms in turbomachines. *Journal of Turbomachinery*. 115: 621–656.

Gaetani P., Persico G., and Osnaghi C. (2010). Effects of axial gap on the vane-rotor interaction in a low aspect ratio turbine stage. *Journal of Propulsion and Power*. 26 (2): 325–334. https://doi.org/10.2514/1.37616.

Grönman A., Turunen-Saaresti T., Röttä P., and Jaatinen-Värri A. (2014). Influence of the axial turbine design parameters on the stator-rotor axial clearance losses. *Journal of Power and Energy*. 228 (5): 482–490. https://doi.org/10.1177/0957650914531949.

Henke M., Biester M. H.-O., Guendogdu Y., Lippl F., Mass E., and Seume J. R. (2012). Numerical Assisted Design of a Variable Rotating Vane Carrier Device for Turbine Test Rigs with Split Housing Structures Using a Segmented Half-Ring Bearing Concept. In: 53rd AIAA/ASME/ASCE/AHS/ASC Structures, Structural Dynamics and Materials Conference. Honolulu: AIAA. https://doi.org/10.2514/6.2012-1660.

Henke M., Wein L., Kluge T., Guendogdu Y., Biester M. H., and Seume J. R. (2016). Experimental and Numerical Verification of the Core-Flow in a New Low-Pressure Turbine. In: ASME Turbo Expo. Seoul: ASME. https://doi.org/10.1115/GT2016-57101.

Jung A. (2000). *Berechnung der Stator-Rotor-Wechselwirkung in Turbomaschinen*. PhD, Universität Stuttgart.

Kato M., and Launder B. E. (1993). The modeling of turbulent flow around stationary and vibrating square cylinders. In: *9th Symposium on Turbulent Shear Flows*. Kyoto. https://doi.org/10.4.1–10.4.6.

Kožulović D., Röber T., and Nürnberger D. (2007). Application of a Multimode Transition Model to Turbomachinery Flows. In: *7th European Conference on Turbomachinery*. Athens: ETC, pp. 5–9.

Mimic D., Sauer P., Oettinger M., and Herbst F. (2019). Shock–Vortex Interaction in a Transonic Turbine Cascade. In: *Global Power and Propulsion Society*, Beijing: GPPS. GPPS-BJ-2019-0008.2019.

Park J., Choi M., and Baek J. (2003). Effects of axial gap on unsteady secondary flow in one-stage axial turbine. *Journal of Turbo and Jet Engines*. 20: 315–333. https://doi.org/10.1515/TJJ.2003.20.4.315.

Pichler R., Michelassi V., Sandberg R., and Ong J. (2017). Highly resolved LES study of gap size effect on low-pressure turbine stage. *Journal of Turbomachinery*. 140 (2). https://doi.org/10.1115/1.4038178.

Praisner T. J., Clark J. P., Nash T. C., Rice M. J., and Grover E. A. (2006). Performance Impacts Due to Wake Mixing in Axial-Flow Turbomachinery. In: *ASME Turbo Expo*. Barcelona: ASME, pp. 1821–1830. https://doi.org/10.1115/GT2006-90666.

Restemeier M., Jeschke P., Guendogdu Y., and Gier J. (2013). Numerical and experimental analysis of the effect of variable blade row spacing in a subsonic axial turbine. *Journal of Turbomachinery*. 135: 2. https://doi.org/10.1115/1.4006587.

Venable B. L., Delaney R. A., Busby J. A., Davis R. L., Dorney D. J., et al. (1999). Influence of vane-blade spacing on transonic turbine stage aerodynamics: Part I—time-averaged data and analysis. *Journal of Turbomachinery*. 121 (4): 663–672. https://doi.org/10.1115/1.2836718.

Wilcox D. C. (1998). *Turbulence Modeling for CFD*. 2nd ed. La Cañada: DCW Industries.

Yamada K., Funazaki K., Kikuchi M., and Sato H. (2009). Influences of Axial Gap Between Blade Rows on Secondary Flows and Aerodynamic Performance in a Turbine Stage. In: *ASME Turbo Expo*. Orlando: ASME, pp. 1039–1049. https://doi.org/10.1115/GT2009-59855.